

Dark Matter Hot Spots and Neutrino Telescopes

Meighen-Berger S.^{a,1}, Karl M.^{a,b}

^a*Technische Universität München, James-Frank-Straße, 85748, Garching, Germany*

^b*Max Planck Institute for Physics, Föhringer Ring 6, 80805 München, Germany*

Abstract

We perform a new dark matter hot spot analysis using ten years of public IceCube data. In this analysis we assume dark matter self-annihilates to neutrino pairs and treat the production sites as discrete point sources. For neutrino telescopes these sites will appear as hot spots in the sky, possibly outshining other standard model neutrino sources. Comparing to galactic center analyses, we show that this approach is a powerful tool and capable of setting the highest neutrino detector limits for dark matter masses between 10 TeV and 100 PeV. This is due to the inclusion of spatial information in addition to the typically used energy deposition in the analysis.

1. Introduction

With new neutrino telescopes under construction, such as P-ONE [1], KM3NeT [2], GVD [3] and IceCube-Gen2 [4] we expect an improving global sky coverage in the coming years. Especially with collaborative efforts, such as PLEνM [5] the sensitivity to point-like objects emitting neutrinos will increase across the entire sky. With these developments in mind, we perform a point source search for self-annihilating dark matter (DM) to study the capabilities of such analyses in the search for new physics.

Multiple dark matter studies using IceCube and or ANTARES have been performed such as the search for dark matter from the center of our galaxy [6, 7, 8]. This can be further expanded upon, by including neutrinos produced by diffuse dark matter in our galactic halo or beyond [9, 10]. Other sources of dark matter signals have been hypothesized and studied as well, such as the sun [11, 12] and the center of the earth [13].

In the scenario that dark matter self-annihilates to a neutrino pair, these sources would possess a distinct energy spectrum, a peak at the dark matter's rest mass. They would also appear as "hot spots" in the sky. These would be well defined regions, as large as the object of interest, where the energy spectrum of the astrophysical neutrino flux would

change compared to the diffuse flux [14]. Especially massive dark matter, with masses above 10 TeV, would cause such a shift. For smaller objects such as suns or planets or even distant galaxies, these hot spots would shrink down to a point. See [15] for an example study on galaxy clusters.

In this letter we utilize this fact and perform a point source analysis for self-annihilating dark matter directly producing neutrinos², using ten years of IceCube public point source data [16, 17].

2. Modelling

For this search there are two primary backgrounds, the atmospheric neutrino flux, as well as the astrophysical diffuse flux. To model the atmospheric flux, we use MCEq [18], a cascade equation approach. As primary, interaction, and atmospheric models we use H4a [19], EPOS-LHC [20] and NRLMSISE-00 [21, 22] respectively. For a comment on other models see Appendix A. To model the astrophysical neutrino flux, we use a single power-law

$$\frac{d\phi}{dE} = \phi_0 \times \left(\frac{E}{100 \text{ TeV}} \right)^{-\gamma}, \quad (1)$$

with $\phi_0 = 1.66_{-0.27}^{+0.25} [10^{-18} \times (\text{GeV} \cdot \text{cm}^2 \cdot \text{s} \cdot \text{sr})^{-1}]$ and $\gamma = 2.53 \pm 0.07$ [14]. We then apply the effective areas and mixing matrices published together

¹stephan.meighen-berger@tum.de

²Code: <https://github.com/MeighenBergerS/dmpoint>

with 10 years of IceCube data [16, 17]. From this we obtain predicted event counts due to the atmospheric and astrophysical flux. In figure 1 we show an example of how a 1 PeV neutrino is reconstructed according to the mixing matrix and effective area. The detector will measure a reconstructed muon and its energy E_{reco} , with the most likely reconstruction energy being approximately at 300 TeV. For this reason even when injecting neutrino lines (in energy) a broad spectrum at lower energies will be measured.

After performing a combined fit on data, where we let the normalization of the fluxes float, we obtain our simulation model for this analysis. The normalization fit results are 1.05 and 1.1 for the atmospheric and astrophysical counts respectively. The fit itself is performed on events above 10 TeV and for a zenith angle $\theta_{\text{zenith}} > 90^\circ$. These values correspond to the energy and angular cuts we introduce when analyzing the data.

In figure 2 we show the resulting predictions compared to data. We use these simulation values to construct energy weights ω_{Energy} later in the analysis. The weights are the ratio between the expected astrophysical and atmospheric events. The point at which we expect the astrophysical flux to dominate is approximately at 200 TeV, at which point $\omega_{\text{Energy}} > 1$.

To model neutrinos produced directly by dark matter self-annihilation we use [9, 23]

$$\frac{d\phi_\nu}{dE_\nu} = \frac{1}{4\pi} \frac{\langle\sigma v\rangle}{2m_\chi^2} \frac{dN_\nu}{dE_\nu} J(\psi), \quad (2)$$

with the produced neutrino spectrum dN_ν/dE defined as

$$\frac{dN_\nu}{dE_\nu} = 2\delta \left(1 - \frac{E_\nu}{m_\chi}\right) \frac{m_\chi}{E^2}. \quad (3)$$

$\langle\sigma v\rangle$ is the thermally averaged self-annihilation cross section, m_χ the dark matter mass, E_ν the resulting neutrino energy and J the integral over the target's solid angle and the dark matter density along the line of sight. Here J has units $\text{GeV}^2\text{cm}^{-5}\text{sr}$. In the above equations we assume Majorana dark matter, which can be changed to Dirac DM by dividing the differential flux by 2. We use the above equations to extract limits on the mass m_χ and the cross section $\langle\sigma v\rangle$ from the calculated flux limits.

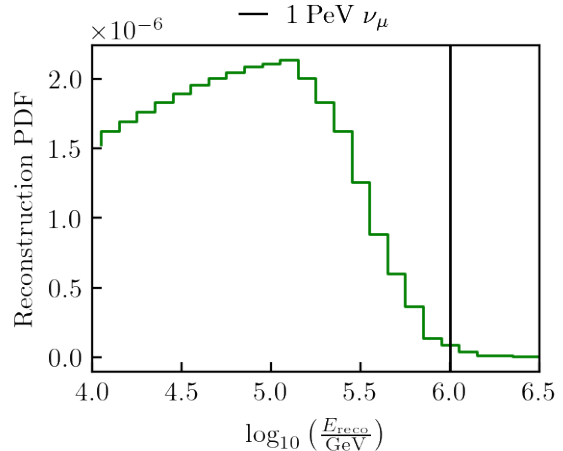


Figure 1: An example, showing how a 1 PeV ν_μ (black line) is reconstructed according to the published effective areas and mixing matrices. In green we show the reconstruction pdf which is sampled when generating signal events.

3. Analysis

To analyze the data we bin the events in energy and spatial position. For the energy grid we use a logarithmic grid with 10 bins per magnitude. In the case of the spatial binning we construct a linear grid with a step size of 0.2° , the minimal resolution of the public data set [16, 17]. As mentioned previously the energy weights ω_{Energy} are the ratio between the expected event counts for the astrophysical and atmospheric neutrinos in each bin.

For the spatial probability distribution function (pdf) we assume a Gaussian distribution \mathcal{N} of the form

$$\omega_{\text{Spatial}}^{\text{Event}}(\delta, \alpha) = \mathcal{N}(r(\delta^{\text{Event}} - \delta, \alpha^{\text{Event}} - \alpha), \text{Error}) \quad (4)$$

Here $r(\delta, \alpha)$ is a distance measure between the event's direction and a point on the grid, with δ and α being the declination and right ascension respectively. Error is the angular reconstruction error of the event. We then assign each spatial grid point a score value \mathcal{S} according to

$$\mathcal{S}(\delta, \alpha) = \sum_i \omega_{\text{Energy}}^i \omega_{\text{Spatial}}^i(\delta, \alpha) \quad (5)$$

where the sum runs over all events, i , in the sample. Figure 3 shows a heat map of the weighted

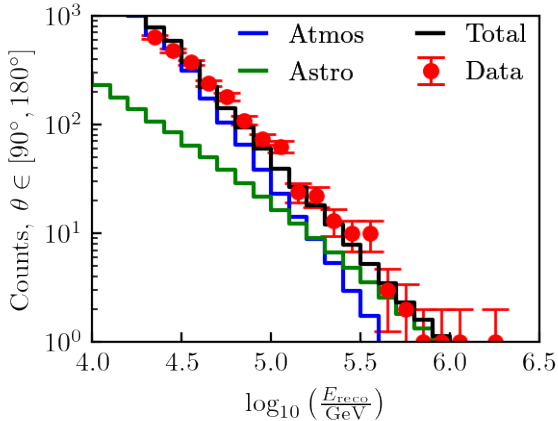


Figure 2: The expected atmospheric and astrophysical counts. We show the individual components in blue (atmospheric) and green (astrophysical). The resulting total counts are given in black and the measured event counts including statistical errors are shown in red. Here we integrated over θ_{zenith} between 90° and 180° .

data events. In white we show the 10° declination band used in the analysis presented here. For higher declinations, we would expect a reduction in sensitivity. This is due to the attenuation of highly energetic neutrinos in the earth.

For the null-hypothesis, we scramble the data in declination. For this analysis, we performed 100000 scrambles and construct the cumulative distribution of the score values. From these we can construct the mean expectation and standard deviations. See the Appendix B for a more detailed discussion on the distribution.

Performing a standard frequentist hypothesis test [24, 25, 26] on the data's distribution we find no significant deviation between the data and the null hypothesis with a p value of 0.4. For details on the confidence limit calculation see the Appendix C.

4. Limits

To keep the constraints as model independent as possible we first inject signal energy fluxes ϕ_{Sig} of the form

$$\phi_{\text{Sig}} = \phi_0 \delta(E - E_{\text{injection}}). \quad (6)$$

We scan $E_{\text{injection}}$ and set constraints on the flux normalization ϕ_0 . We assume the angular uncertainty on the signal events lies between 0.5° and

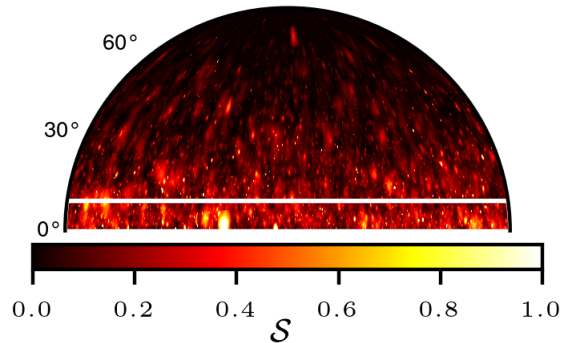


Figure 3: The density sky map after weighting and folding with the spatial pdf. The region below the white line is used for this analysis. The plot is made using a Mollweide projection. The color bar describes the score value for each bin. Here we use a cut-off for the maximal score value \mathcal{S} of one.

1° degrees. Together with equation 2 and the modelling procedure described in section 2, we construct the expected events. Here we analyze four different population hypothesis: 1, 10, 100, and 1000 sources distributed randomly in the area of interest. For each hypothesis we run 100000 simulations and construct the 90% confidence limit. Figure 4 shows the resulting limits compared to the astrophysical diffuse flux. For a single source it may emit more than we expect from the diffuse flux while for $N_{\text{pop}} > 10$ each object needs to emit less. The ratio between these limits is nearly linear.

Until now we have assumed, that we are searching for sources emitting spectral neutrino lines. A natural choice to compare our current results with are those derived for the galactic center. To make this comparison, we need to construct limits on dark matter specific to equation 2 and set $J(\psi)$. From [6, 23] we can construct a conservative estimate for a NFW profile [27] of $1e24 \text{ GeV}^2 \text{ cm}^{-5} \text{ sr}$, using an angular reconstruction error of 1° . Including IceCube's sensitivity dependence on declination, we reduce this value by a factor of 10 [16], to account for the galactic center being in the southern sky ($\delta \approx -30^\circ$). With this we convert the flux limits from figure 4 to ones on the thermally averaged self-annihilation cross section $\langle \sigma v \rangle$ and the dark matter mass m_χ . Figure 5 shows the results. There we also show the limits presented in [9] for IceCube and ANTARES [28, 29] as a comparison. The limit we set here for a single point source is more strin-

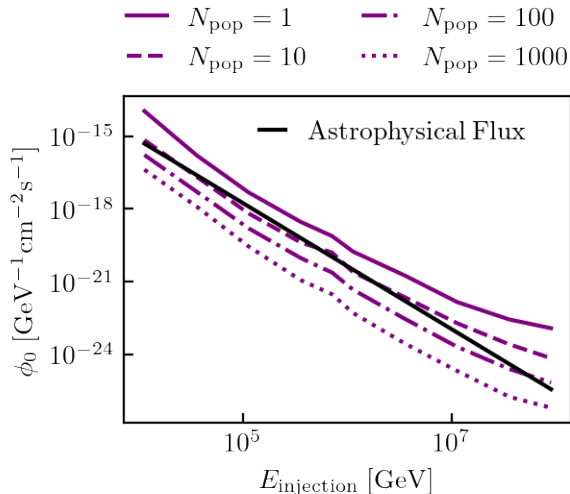


Figure 4: 90% CL limits for differing number of populations. Here we show the absolute flux limit for a given injection energy. The solid black line depicts the astrophysical diffuse flux as a comparison. It is given in $\text{GeV}^{-1} \text{cm}^{-2} \text{s}^{-1} \text{sr}^{-1}$. The extracted flux limits are depicted using the purple solid ($N_{\text{pop}} = 1$), dashed ($N_{\text{pop}} = 10$), dotted-dashed ($N_{\text{pop}} = 100$) and dotted ($N_{\text{pop}} = 1000$) lines.

gent than the previous IceCube study, due to the inclusion of spatial information in the analysis. The limits then become stronger for larger populations, with $N_{\text{pop}} > 1000$ being mostly excluded when considering the thermal relic abundance. These limits scale linearly with the J -factor. For this reason the presented limits would only improve when moving away from our conservative assumptions.

5. Conclusion

We presented a new search for dark matter including spatial information in addition to the typically analyzed energy distributions. By employing a hot spot population analysis on ten years of public IceCube data, we were able to set limits on self-annihilating dark matter over a broad energy range. We compared the method to previous limits on dark matter in our galaxy. In our comparison we would set the most stringent neutrino telescope constraints on self-annihilating dark matter with masses between 10 TeV and 10 PeV coming from the galactic center. In this picture, we were able to push the bounds on large populations of dark matter sources $N_{\text{pop}} > 1000$ below the thermal relic abundance. In the future we expect

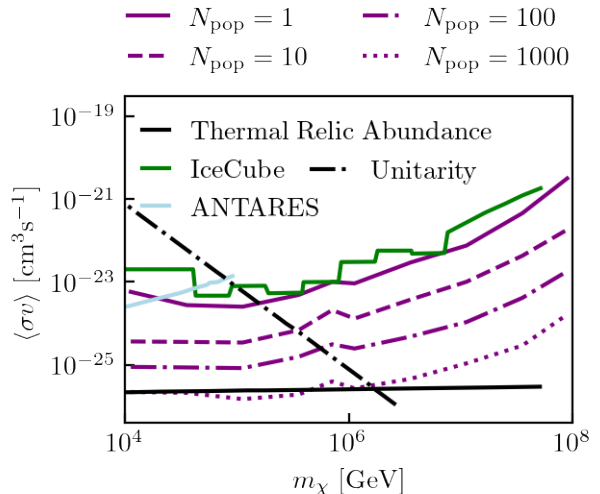


Figure 5: DM limits assuming $J(\psi) = 1e23 \text{ GeV}^2 \text{cm}^{-5} \text{sr}$. Here we compare the limits to those for IceCube from [9] (green) and ANTARES [28, 29] (light blue). We show the extracted limits using the purple solid ($N_{\text{pop}} = 1$), dashed ($N_{\text{pop}} = 10$), dotted-dashed ($N_{\text{pop}} = 100$) and dotted ($N_{\text{pop}} = 1000$) lines. All of the limits follow a similar shape, with the ones presented here scaling nearly linearly with population. We include the constraints set by unitarity (black, dashed dotted) on non-composite dark matter [30, 9] and the thermal relic abundance (black, solid) [9].

this method to only improve. Besides the new neutrino telescopes currently being constructed, such as KM3NeT, GVD and P-ONE, this method would only benefit once an actual neutrino source has been discovered. With the evidence of a point source already found with TXS 0506+056 [31], we expect this to happen in the coming years. For this reason we suggest not only using point source searches for astrophysical goals, instead to also employ them in the search for new physics.

References

- [1] M. Agostini et al. (P-ONE), *Nature Astron.* **4**, 913 (2020), 2005.09493.
- [2] S. Adrian-Martinez et al. (KM3Net), *J. Phys.* **G43**, 084001 (2016), 1601.07459.
- [3] A. D. Avrorin et al., *EPJ Web Conf.* **136**, 04007 (2017).
- [4] J. van Santen (IceCube Gen2), *PoS ICRC2017*, 991 (2018).
- [5] L. J. Schumacher, M. Huber, M. Agostini, M. Bustamante, F. Oikonomou, and E. Resconi, *PoS ICRC2021*, 1185 (2021), 2107.13534.
- [6] M. G. Aartsen et al. (IceCube), *Eur. Phys. J. C* **75**, 492 (2015), 1505.07259.

- [7] M. G. Aartsen et al. (IceCube), *Eur. Phys. J. C* **77**, 627 (2017), 1705.08103.
- [8] A. Albert et al. (ANTARES, IceCube), *Phys. Rev. D* **102**, 082002 (2020), 2003.06614.
- [9] C. A. Argüelles, A. Diaz, A. Kheirandish, A. Olivares-Del-Campo, I. Safa, and A. C. Vincent (2019), 1912.09486.
- [10] C. El Aisati, C. Garcia-Cely, T. Hambye, and L. Vanderheyden, *JCAP* **10**, 021 (2017), 1706.06600.
- [11] C. A. Argüelles, A. Kheirandish, J. Lazar, and Q. Liu (IceCube), *PoS ICRC2019*, 527 (2021), 1909.03930.
- [12] C.-S. Chen, F.-F. Lee, G.-L. Lin, and Y.-H. Lin, *JCAP* **10**, 049 (2014), 1408.5471.
- [13] R. Abbasi et al. (IceCube), *PoS ICRC2019*, 541 (2020), 1908.07255.
- [14] M. G. Aartsen et al. (IceCube), *Phys. Rev. Lett.* **125**, 121104 (2020), 2001.09520.
- [15] K. Murase and J. F. Beacom, *JCAP* **02**, 028 (2013), 1209.0225.
- [16] M. G. Aartsen et al. (IceCube), *Phys. Rev. Lett.* **124**, 051103 (2020), 1910.08488.
- [17] R. Abbasi et al. (IceCube) (2021), 2101.09836.
- [18] A. Fedynitch, R. Engel, T. K. Gaisser, F. Riehn, and T. Stanev, *EPJ Web Conf.* **99**, 08001 (2015), 1503.00544.
- [19] T. K. Gaisser, *Astropart. Phys.* **35**, 801 (2012), 1111.6675.
- [20] T. Pierog, I. Karpenko, J. M. Katzy, E. Yatsenko, and K. Werner, *Phys. Rev. C* **92**, 034906 (2015), 1306.0121.
- [21] A. E. Hedin, *Journal of Geophysical Research: Space Physics* **96**, 1159 (1991), <https://agupubs.onlinelibrary.wiley.com/doi/pdf/10.1029/90JA02125>, URL <https://agupubs.onlinelibrary.wiley.com/doi/abs/10.1029/90JA02125>.
- [22] J. M. Picone, A. E. Hedin, D. P. Drob, and A. C. Aikin, *Journal of Geophysical Research: Space Physics* **107**, S1A 15 (2002), <https://agupubs.onlinelibrary.wiley.com/doi/pdf/10.1029/2002JA009430>, URL <https://agupubs.onlinelibrary.wiley.com/doi/abs/10.1029/2002JA009430>.
- [23] H. Yuksel, S. Horiuchi, J. F. Beacom, and S. Ando, *Phys. Rev. D* **76**, 123506 (2007), 0707.0196.
- [24] G. J. Feldman and R. D. Cousins, *Phys. Rev. D* **57**, 3873 (1998), physics/9711021.
- [25] A. L. Read, *J. Phys. G* **28**, 2693 (2002).
- [26] F. James, Y. Perrin, and L. Lyons, *CERN Yellow Reports: Conference Proceedings* **5** (2000).
- [27] J. F. Navarro, C. S. Frenk, and S. D. M. White, *Astrophys. J.* **462**, 563 (1996), astro-ph/9508025.
- [28] S. Adrian-Martinez et al. (ANTARES), *JCAP* **10**, 068 (2015), 1505.04866.
- [29] A. Albert et al., *Phys. Lett. B* **769**, 249 (2017), [Erratum: *Phys.Lett.B* 796, 253–255 (2019)], 1612.04595.
- [30] J. Smirnov and J. F. Beacom, *Phys. Rev. D* **100**, 043029 (2019), 1904.11503.
- [31] M. G. Aartsen et al. (IceCube), *Science* **361**, 147 (2018), 1807.08794.
- [32] J. F. Beacom, N. F. Bell, and G. D. Mack, *Phys. Rev. Lett.* **99**, 231301 (2007), astro-ph/0608090.
- [33] F. Riehn, H. P. Dembinski, R. Engel, A. Fedynitch, T. K. Gaisser, and T. Stanev, *PoS ICRC2017*, 301 (2018), 1709.07227.
- [34] S. Ostapchenko, *Phys. Rev. D* **83**, 014018 (2011), 1010.1869.
- [35] S. Roesler, R. Engel, and J. Ranft, SLAC-PUB-8740

(2000), hep-ph/0012252.

- [36] T. K. Gaisser, T. Stanev, and S. Tilav, *Front. Phys. (Beijing)* **8**, 748 (2013), 1303.3565.

Appendix A. Atmospheric Shower Differences

To understand the dependence of this analysis on the primary and interaction models used in simulating atmospheric showers, we perform the analysis with other models as well. In the case if the interaction model, we also test Sibyll 2.3c [33], QGSJET-II [34] and DPMJET-III [35]). For the primary models we use H3a [19] as well as and Gaisser-Stanev-Tilav Gen 3 and 4 [36]. Running the analysis we found the differences for the final results negligible. The reason for this is the fit to data we perform in the analysis described in section 2.

Appendix B. Cumulative Distribution

The cumulative distribution function of the score value \mathcal{S} used in the evaluation, described above. The background model (black) was constructed by scrambling the data 100000 in right ascension. The green and yellow regions mark the one and two σ confidence intervals from the background model. The distribution $\mathcal{D}(\mathcal{S})$ itself is constructed

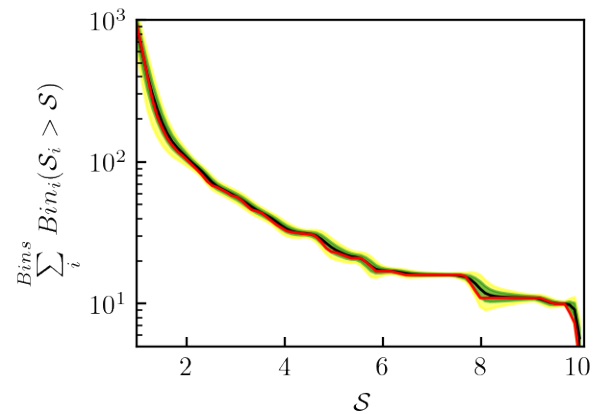


Figure B.6: The measured cumulative distribution (red) compared to the mean from the scrambled ones (black). In green and yellow we respectively show the 1σ and 2σ confidence intervals of the scrambled sets. Note that the data agrees well with the null-hypothesis. This means there are no significant deviations from a diffuse background assumption.

by counting the number of spatial grid points (bins)

with a score value \mathcal{S}_i above a given value \mathcal{S}

$$\mathcal{D}(\mathcal{S}) = \sum_i^{Bins} Bin_i(\mathcal{S}_i > \mathcal{S}). \quad (\text{B.1})$$

Appendix C. Limit Setting

To construct the limits on the new flux we perform a frequentist analysis using the CL(s) technique [25, 26]. CL_s is defined as the ratio of the signal + background hypothesis CL_{s+b} and the background only hypothesis CL_b (the left sided p-values of the test statistic distribution):

$$CL_s = \frac{CL_{s+b}}{CL_b}. \quad (\text{C.1})$$

From this the confidence limit is defined as

$$1 - CL_s \leq CL. \quad (\text{C.2})$$

We define the test statistic Q as

$$Q = \frac{\prod_{i=1}^{N_{\text{bins}}} \mathcal{P}(n_i, s_i + b_i)}{\prod_{i=1}^{N_{\text{bins}}} \mathcal{P}(n_i, b_i)}, \quad (\text{C.3})$$

where the product runs over the bins and \mathcal{P} is the Poisson probability mass function. n_i , s_i and b_i are the observed, signal and background score values respectively. To calculate CL_s this test statistic needs to be constructed for the signal + background and background only hypothesis. The background expectations b_i are constructed using the mean of the 100000 data scrambles.